Ocean Engineering 282 (2023) 115005

Contents lists available at ScienceDirect

Ocean Engineering

journal homepage: www.elsevier.com/locate/oceaneng

Towards autonomous contact-free operations in aquaculture

Martin Albertsen Brandt [a,*], Sverre Herland [b], Martin Gutsch [c], Halgeir Ludvigsen [c], Esten Ingar Grøtli [a]

[a] Department of Mathematics and Cybernetics, SINTEF Digital, Trondheim, Norway
[b] Department of Computer Science, Norwegian University of Science and Technology, Trondheim, Norway
[c] Department of Ships and Ocean Structures, SINTEF Ocean, Trondheim, Norway

ARTICLE INFO

Keywords:
Exposed aquaculture
Offshore fish farming
Remote operations
Motion compensation
Vessel motion simulation
Robot manipulator arm

ABSTRACT

As offshore fish farms are established farther away from the shore, increased exposure to the elements prevents regular operations from being performed safely with vessels moored alongside the flexible fish cage and personnel performing tasks standing on the collar. Due to the higher environmental impact at more exposed locations, new concepts and solutions for automating daily aquaculture operations need to be developed. One solution that has been proposed is to carry out operations using a robotic arm mounted on the main deck of a service vessel while it does stationkeeping next to the cage. The purpose of this article is to summarise our research on the viability of this concept. Vessel motions are simulated for a representative vessel model and realistic sea states, and a robotic arm does motion-compensated trajectory tracking while mounted on a hexapod platform moving according to the simulated vessel motions. Relevant challenges in marine aquaculture operations are summarised, the method used to obtain realistic simulated vessel motions is documented, the results of the experiments are presented, and the remaining open questions to evaluate the potential of the proposed system are discussed.

1. Introduction

Aquaculture operations are performed by three different vessel classes; wellboats for storage and transport of live fish, feed carriers, and service vessels (Bjelland et al., 2015). Traditionally, the majority of work tasks were executed by small vessels, moored alongside the flexible fish cage structure to allow the personnel to perform their work tasks physically standing on the collar of the fish cage. While service vessels are used for maintenance work and support tasks at the fish cages on a daily basis, larger vessels, such as wellboats, are sporadically moored to the fish cage when fish are treated, or to be transported or moved between cages. Feed carriers rather dock to the feeding barge to replenish supplies and are not operating directly by the fish cage.

Until 2015, the length of aquaculture service vessels in Norway was kept below 15 m to avoid formal educational requirements of the captain. During this time the service operation vessel, typically designed as twin-hull work vessels, increased in width to provide sufficient deck space without increasing its length (Ramm and Berge, 2017). However, since the Norwegian Maritime Authority changed rules (Norwegian Ministry of Trade, Industry and Fisheries, 2015), the qualification requirements of offshore personnel were defined more independently of vessel size, and the fishing industry started to introduce larger service vessels to the market. These larger vessels are supposed to provide better seakeeping performance, which is essential when moving fish production to more exposed locations.

Harsher weather conditions in terms of increased wave height, wind, and current lead to larger environmental loads on the vessel and make the direct interaction between the vessel and cage structure more challenging and hazardous, both in terms of the structural integrity of the facility and health, safety, and environment (HSE) (Holmen et al., 2017; Bjelland et al., 2015). Therefore, depending on vessel size, the traditional procedure of mooring the vessel alongside the collar becomes unfeasible.

While salmon and trout farming in Norway began in well-sheltered coastal environments, today the industry lacks such areas, both due to competition with other coast-based industries such as tourism and fishing, and due to the large growth that the salmon industry has seen in recent decades (Bjelland et al., 2015). This has led to a move towards more exposed locations, where operational windows are shorter and more irregular due to harsher environmental conditions. To enforce and regulate workplace HSE concerns, it is proposed to evaluate if operations, especially those of critical regularity, can be executed without the need of moving people onto the cage itself. Utne et al. (2017) presented a mapping of HSE risks in exposed aquaculture operations,

* Corresponding author.
E-mail address: martin.brandt@sintef.no (M.A. Brandt).

https://doi.org/10.1016/j.oceaneng.2023.115005
Received 8 July 2022; Received in revised form 2 March 2023; Accepted 20 March 2023
Available online 11 June 2023

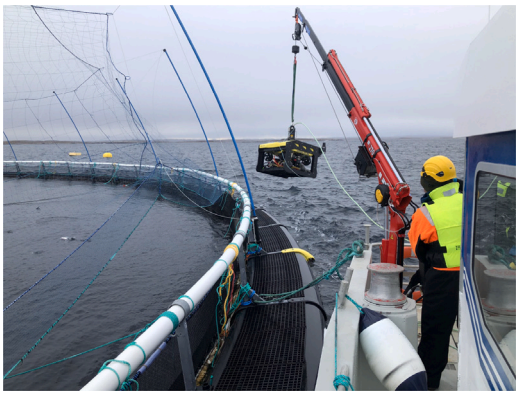

Fig. 1. Exemplary image of manual ROV launch and recovery operation.

stating that it is one of the most dangerous occupations in Norway. In this context, a need for contact-free aquaculture operations where the service vessel is not moored to the cage, i.e., with no direct contact between the vessel and the fish cage, is identified. For this purpose, a dynamic positioning (DP) system shall maintain the vessel's position and orientation, by using reference positions at the fish cage. For safety reasons, with regards to the integrity of the cage and fish welfare, the operational planning, proximity sensors, and system redundancy must guarantee a minimum distance between vessel and fish cage and the net below water surface.

In Misund and Gutsch (2020) a number of operations in and around fish cages were identified (provided in Appendix). Operations are carried out with varying regularity and number of personnel involved. These operations include a number of regular inspection and maintenance tasks that can be supported by using cranes, such as dead fish removal, net maintenance, and fish health monitoring. All these operations require personnel physically standing on the collar. Additionally, for net maintenance and cleaning, small remotely operated vehicles (ROVs) are launched and recovered by cranes mounted on the vessel moored to the collar. An example of this is shown for a smaller vessel in Fig. 1.

Typically, an ROV inspection operation consists of the following steps: create an opening in the bird net covering the cage, place the ROV inside the cage through the opening, perform the inspection with the ROV, retrieve the ROV, and close the opening in the bird net. One question to be answered is how to sense and interact with the cage. Service vessels are typically equipped with cranes, and today they are used for launch- and recovery of ROVs. However, cranes lack accurate actuation in all degrees of freedom (DOF). Large robotic arms are proposed as an alternative in this paper. Such robotic arms mounted on the vessel, are, for instance, used for mooring operations at Yara Birkeland,[1] the first autonomous cargo ferry in commercial operations.

Tracking and planning with robotic arms and cranes have been extensively studied in the literature. A relevant example is presented by Faulwasser et al. (2017), who considers real-time path-following for industrial robots using nonlinear model predictive control. The authors present results with a 7 DOF robot manipulator drawing a predetermined path on a whiteboard. However, they do this from a stationary robot base. Problems and experimental approaches involving non-stationary robot bases introduce an additional set of challenges as they work in non-inertial coordinate frames (Cao and Li, 2020). Non-controllable base motions are typically found when robotic arms and cranes are fixed to floating structures such as the deck of a vessel. In such cases, the actuated joints will have to compensate for disturbances in uncontrolled DOF. From et al. (2011) modelled vessel motions and use predictions of future motion during planning for vessel-mounted robot manipulators. They test on a 9 DOF test rig, of which the first 5 DOF are used to emulate the vessel motion (sway/heave/roll/pitch/yaw) and the latter 4 DOF are used as the robotic arm. Sun et al. (2018) consider ship-mounted cranes under the influence of just roll and heave motion. They construct a Lyapunov-based control law for suppressing swing in suspended cargo without linearising or approximating the nonlinear dynamics and verify the proposed solution on an in-lab test rig. A similar problem is addressed by Tysse et al. (2022), who propose another Lyapunov-based controller to stabilise the pendulum dynamics of the crane payload and validate it on a small-scale stationary knuckle boom crane. Tørdal and Hovland (2017) considers motion compensation for vessel-to-vessel load handling with cranes. They used an inverse-kinematics-based controller to compensate for heave, roll, and pitch while keeping the end effector at a fixed height from the deck of another vessel. The solution is tested on a robotic arm and two hexapods that follow wave motions sampled from the Pierson–Moskowitz (PM) spectrum. Although the experiment is performed at full scale, the significant wave height of the PM spectrum is down-scaled to a significant wave height of $H_S = 0.4\,\mathrm{m}$ to accommodate the limited stroke length of the equipment. This leads to a swell-like sea-state with low accelerations, which is less interesting from an operational point of view.

In this paper, an experimental feasibility study of contact-free operations is presented using a vessel-mounted robotic arm. The system is experimentally verified with a robotic arm mounted on a moving hexapod platform. To summarise our main contributions are:

- A description and study of a novel concept where a robotic arm is used in offshore aquaculture operations.
- A realistic, full 6 DOF motion simulation of a representative service vessel operating under DP in sea states typical at aquaculture sites. The sea states have varying intensity between $H_S = 0.5\,\mathrm{m}$ and $H_S = 2\,\mathrm{m}$, and peak wave period in the range of $T_p = 6\,\mathrm{s}$ to $T_p = 9\,\mathrm{s}$.
- Investigation of the influence of scaling to an experimental setup suited for this concept. Froude scaling was used to ensure that accelerations and thus gravity and mass forces are correctly scaled to preserve accelerations of a full-scale experiment.
- Experimental test of the feasibility of motion compensation and trajectory tracking in a scaled experiment. Vessel motions centred around the base of the robotic arm are extracted and simulated by the hexapod platform in a scaled manner. Coordinate frames of relevant objects are tracked using motion capture, and trajectory tracking is achieved by calculating the desired end effector pose in real time.
- Evaluation of 6 DOF end effector reference trajectory tracking. Results are presented and analysed, and a discussion of challenges and open problems is provided.

The remainder of the paper is organised as follows. In Section 2 the vessel, sea state, and DP models used to generate the simulated vessel motions are presented. The experimental setup and control task are presented in Section 3. Results from four scaled down experiments with differing sea states are presented in Section 4. The findings and limitations of the results, open problems, and further research directions are discussed in Section 5. Section 6 concludes the paper.

2. Vessel motion simulations

2.1. Vessel model

AQS Loke,[2] shown in Fig. 2, was used as a case vessel in the presented study. With a length of 25.5 m and a beam of almost 12.0 m,

[1] https://www.macgregor.com/intelligent-solutions/automated-mooring-system/.

[2] https://aqs.no/vessels/aqs-loke/.

Fig. 2. Aquaculture service vessel AQS Loke.

Table 1
Adapted loading condition. Draught refers to the draught midship.

Draught [m]	GM_T [m]	VCG [m]	R_{44} [m]	R_{55} [m]
2.20	8.27	2.90	5.36	6.09

the vessel was at the time of commissioning the largest and most modern aquaculture service vessel in operation in Norway (Ramm and Berge, 2017). This vessel was chosen since it represents a modern vessel typically used in the aquaculture industry, of sufficient size for the types of operations considered here. The vessel was modelled as it is in operation, and no further modifications were made to optimise it.

Response amplitude operators (RAOs) with respect to the centre of gravity (COG) were calculated with the 2D linear strip theory vessel response calculation software VERES (Salvesen et al., 1970; Fathi, 2012) along with the 3D potential vessel motion analysis software WAMIT.[3] The purpose of combining these tools for the calculation of the vessel response model is to utilise the frequency-dependent added mass and damping, as well as wave drift forces, from WAMIT while VERES allows to more correctly estimate the viscous roll damping contributions.

VERES calculates viscous roll damping from hull friction and vortex damping due to frictional shear stress on the hull surface (Kato, 1957). Further, eddy damping (Ikeda et al., 1977) and lift damping from pressure variation, along the naked hull, (Himeno, 1981) are included. Wave radiation damping at zero speed is obtained from the analysis of each single strip. Contributions of non-linear viscous damping effects are included for a wave amplitude of 1.25 m in a linear fashion.

The wave motion calculations encompass the following parameters:

- One loading condition (see Table 1).
- Zero speed.
- Wave heading of 150° (relating to port-side stern quartering waves).
- Wave periods calculated from 3 s to 60 s.
- Linear 6 DOF motion RAOs with respect to COG.

For the definition of the vessel load condition as presented in Table 1, the transverse metacentric height GM_T, the vertical centre of gravity VCG, radii for gyration for roll R_{44} and pitch R_{55} are specified. The vessel motion RAOs at COG for quarterly following waves, specified as a wave angle related to head waves of 150°, are presented in Fig. 3 for 3 s to 20 s. The longitudinal, transverse, and vertical motions are denoted surge, sway, and heave, while rotations about the longitudinal, transverse, and vertical axis are denoted roll, pitch, and yaw, respectively. The translational motions surge, sway, and heave are presented as displacement amplitude divided by the (single) amplitude of the incident regular wave (unit amplitude $\zeta_a = 1.0$ m). The rotational

[3] https://www.wamit.com/.

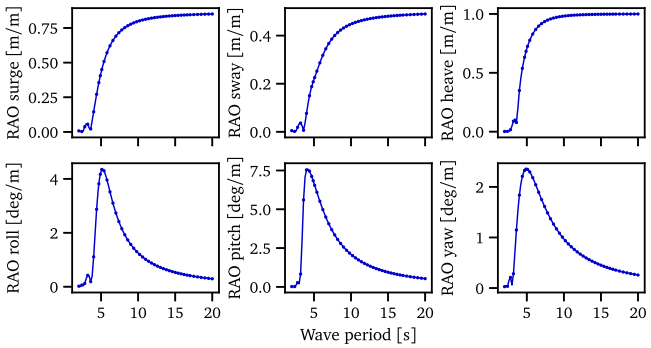

Fig. 3. Vessel motion RAOs for 150° wave angle at zero speed.

Table 2
Parameters for wave spectrum used for the vessel motion simulations.

	H_S [m]	T_p [s]	γ
EXP1	0.5	6.0	3.3
EXP2	1.0	6.0	3.3
EXP3	1.5	8.0	3.3
EXP4	2.0	9.0	3.3

motions roll, pitch, and yaw are presented as motion amplitude divided by the wave slope.

2.2. Environmental model

The vessel motions were simulated in a colinear environment applying the following parameters:

- Long-crested JONSWAP wave spectrum with significant wave height H_S, peak wave period T_p and peak enhancement factor γ, as given in Table 2.
- Constant current speed of 0.5 m/s.
- 100 m water depth.

Exposed fish farm locations in Norway may experience significant wave heights up to 2.5 m and 1.0 m/s mean current velocity (Utne et al., 2017). This makes the chosen range of wave heights in Table 2, representative of environmental conditions that range from sheltered environments to typical conditions at exposed locations. Four different environmental conditions were simulated, labelled EXP1-4. The wave height to period combinations of the chosen sea states reflect a typical undisturbed wind-sea. Such relatively steep waves can be generally regarded as most demanding for smaller vessels.

2.3. Simulations

The simulations were performed using SIMO, a simulator that is a part of the SIMA workbench. SIMA allows the user to establish a simulation model consisting of the vessel motions characterised by vessel RAOs, wave drift, wind and current coefficients, propulsion forces including a DP controller, etc.

The vessel was located in close proximity to a fish cage. The fish cage motions were calculated using the fishery and aquaculture simulator FhSim (Reite et al., 2014) and imported into the SIMA workbench. A point on the collar of the cage was used as reference for the DP controller. The motions of the robot base were exported to be used in the subsequent experiments in Section 3. The robot base was positioned in the starboard quarter of the vessel, as seen visualised in simulation in Fig. 4. The motions are summarised by the motion statistics given in Table 3 and the footprint plots in Fig. 5. The data shown in Table 3 provide the standard deviation, as well as the

Table 3
Motion statistics for simulation of robot base mounted on vessel. The minimum, maximum and standard deviation of the motion trajectory is given for all 6 DOF.

	Surge [m]			Sway [m]			Heave [m]			Roll [deg]			Pitch [deg]			Yaw [deg]		
	min	max	std	min	max	std	min	max	std	min	max	std	min	max	std	min	max	std
EXP1	−0.32	0.32	0.08	−0.26	0.24	0.07	−0.68	0.65	0.17	−1.20	1.27	0.31	−3.02	2.87	0.76	−1.52	1.24	0.35
EXP2	−1.42	0.83	0.32	−0.81	1.53	0.33	−1.36	1.29	0.35	−2.45	2.62	0.61	−6.05	5.74	1.52	−8.12	3.93	1.74
EXP3	−1.32	1.42	0.41	−1.17	1.16	0.37	−1.87	1.67	0.48	−2.22	2.48	0.59	−6.73	6.61	1.78	−6.81	5.40	1.80
EXP4	−1.93	2.37	0.59	−1.87	1.41	0.53	−2.03	2.35	0.61	−2.90	2.41	0.64	−8.59	7.26	2.07	−7.95	8.11	2.44

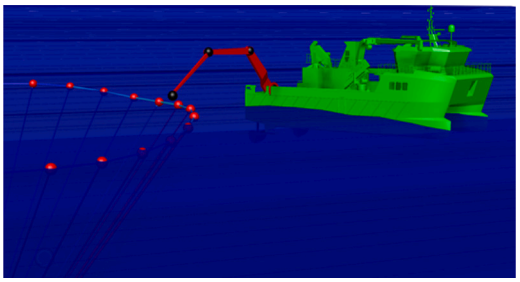

Fig. 4. SIMO model of AQS Loke vessel performing operations close to a fish cage.

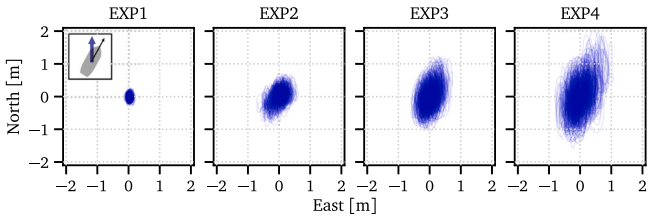

Fig. 5. Robot base DP footprint in the North-East frame, for the four simulated sea states. The wave and current direction points northwards (blue arrow), and is 30° off the vessel heading (black arrow), corresponding to stern quartering seas.

sample minima and maxima of vessel motions used in the experiments. The presented motion statistics give an impression of how the vessel motion increases for higher sea states. The generated motions of the vessel are the response on the non-stationary realisation of the irregular waves. Without DP, the minimum and maximum responses would be Rayleigh distributed. With a DP system, as is the case in the presented study, the maxima responses are somewhere in-between a Rayleigh distribution and Exponential distribution. Thus, in comparison to the standard deviation values, the maxima are somewhat higher than what would be expected for a Rayleigh distribution.

2.4. DP model

SIMO contains a DP controller within the real-time (or faster) time-domain marine operation simulator. The software further includes modules for calculating 6 DOF vessel motions based on, e.g., motion RAOs, as well as external force estimators for wind, waves, current, propulsion, anchor lines, and more. The propulsion library in SIMO consists of hydrodynamic propulsion models for:

- A selection of actuators controlling rotational speed and thrust direction.
- Thruster–thruster interaction effects.
- Thruster–hull interaction effects.
- Thrust losses due to ventilation.

The thrusters were modelled using SIMO 4.1 formulations for a conventional propulsion system and tunnel thrusters. Thruster losses due to thruster–hull interaction were added for the tunnel thrusters. These losses were best-guesses based on previous experience from model testing and were chosen rather high to provide a slightly conservative result. Due to the arrangement of the tunnel thrusters blowing straight into each-other, thruster–thruster interaction losses were additionally included for the tunnel thrusters.

2.5. Scaling

Sufficient reach of the vessel-mounted robotic arm is required to perform contact-free work tasks on a fish cage, while the vessel keeps a safe distance to the cage net. A simple calculation was done to determine a suitable reach. Firstly, a minimum vessel clearance to the cage of 3 m was assumed to be sufficient to allow for vessel excursions due to the size of the DP footprint. Furthermore, the collar width is typically around 1 m, and can be as large as 1.5 m.[4] Finally, a minimum available reach inside the cage of 2 m is required to safely perform operations such as ROV launch and recovery. Given these requirements and adding some extra reach for flexibility, a reach of 8 m was deemed feasible. Based on the size of the robotic arm described in Section 3.1 and with the aim of applying moderate scaling, a scaling factor of $\lambda = 4.84$ was used.

When performing model testing in the marine technology sector, Froude similarity is typically used to assure an equal ratio between the hydrodynamic inertia force F_i and the viscous force F_v:

$$\frac{F_i}{F_v} \propto \frac{\rho U^2 L^2}{\rho g L^3} = \frac{U^2}{gL}, \tag{1}$$

where U is the relative flow velocity and L is the characteristic length. The dynamic similarity requirement between model M and full scale F leads to:

$$\frac{{U_M}^2}{gL_M} = \frac{{U_F}^2}{gL_F}. \tag{2}$$

The ratio of flow inertia to the external gravity field is defined as the Froude number:

$$\frac{U_M}{\sqrt{gL_M}} = \frac{U_F}{\sqrt{gL_F}} = F_n. \tag{3}$$

In marine hydrodynamic applications, the Froude number is an important parameter with respect to the ship's drag, or resistance, especially in terms of wave-making resistance. To obtain Froude similarity, velocity, and thus dependent parameters such as time, are scaled by:

$$\frac{U_M}{U_F} = \frac{\sqrt{gL_M}}{\sqrt{gL_F}} = \sqrt{\lambda}. \tag{4}$$

This scaling method will make sure that accelerations, and thus gravity and mass forces, are correctly scaled, which might be of interest for this type of experiment. However, this scaling method leads to increased translational and rotational speeds, as well as acceleration, leading to additional challenges regarding the responsiveness of the control system. The alternative of not scaling time, on the other hand, would result in an unrealistic low translational speed in model scale.

[4] https://scaleaq.com/product-category/pen-net-and-mooring/pens/.

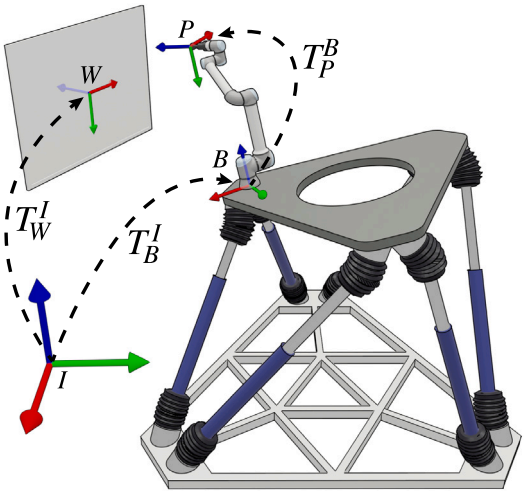

Fig. 6. Experimental setup with Sirocco motion hexapod, UR10e robotic arm and whiteboard. The inertial frame I, robot base frame B, whiteboard frame W and pen tool frame P are annotated, in addition to relevant transforms between these. Red, green and blue arrows indicate x, y and z axes, respectively.

3. Experimental setup

3.1. Hardware

The setup for the lab experiment is illustrated in Fig. 6. A Symétrie[5] Sirocco motion hexapod with a maximum payload of 2 tons was used to generate the scaled simulated vessel motions described in Section 2. A Universal Robots[6] UR10e robot manipulator arm was mounted on the hexapod. The manipulator has a payload capacity of 10 kg and reach of 1.3 m. Furthermore, a 3D-printed end effector with a spring-loaded pen was attached to the robotic arm to draw on a whiteboard. A Qualisys[7] motion capture (MOCAP) system was used to track the robot base in real time. Specifically, four Arqus 12 cameras were used, running at a frequency of 100 Hz. Reflective markers were added to the whiteboard and the robot base, and were tracked as 6 DOF rigid bodies in the Qualisys Track Manager (QTM) software.

3.2. Control task and related transforms

To demonstrate the ability of the system to follow an arbitrary pose trajectory in the presence of waves, we consider the task of drawing a predefined path on a fixed whiteboard with desired speed v_d. The transforms relevant to this task are illustrated in Fig. 6. T_B^I denotes the transform of the robot base frame B relative to the inertial frame I. T_P^B denotes the transform of the pen tool frame P, with origin at the tip of the pen, relative to the robot base frame. Finally, T_W^I denotes the fixed transform of the whiteboard frame W, relative to the inertial frame.

The desired pose trajectory of the pen tool is given in the whiteboard frame by the translation vector $r_{WP^\star}^W$ and rotation matrix $R_{P^\star}^W$. The corresponding homogeneous transformation matrix is denoted by $T_{P^\star}^W$. Here, $P^\star$ denotes the desired pen tool frame, as opposed to the actual pen tool frame P. Finally, the desired pen tool pose trajectory in the robot frame is computed as:

$$T_{P^\star}^B = T_B^{I^{-1}} T_W^I T_{P^\star}^W . \tag{5}$$

[5] https://symetrie.fr/.
[6] https://universal-robots.com/.
[7] https://qualisys.com/.

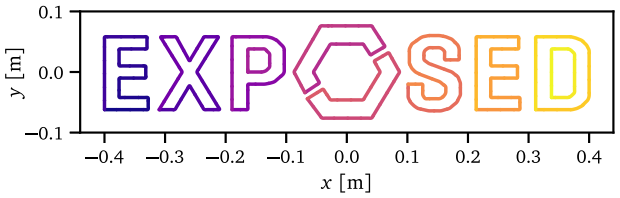

Fig. 7. End effector position reference in the xy-plane of the whiteboard.

The desired pose $T_{P^\star}^B$ is computed at every time step using the measured transforms from the motion capture system and passed to the internal task space controller of the UR10e robotic arm.

Trajectory blending was used to achieve a smooth approach trajectory towards the whiteboard from the initial configuration of the robot. A quintic polynomial with zero initial and final derivatives was used to blend between the initial configuration of the robot and the start pose of the trajectory, using linear interpolation for the position of the end effector and SLERP (Shoemake, 1985) interpolation for the rotation of the end effector.

3.3. Calibration

The transform from the robot base frame to the pen tool frame, T_P^B, consists of a transform from the robot base to the robot flange given by the forward kinematics of the robot, and a fixed transform from the flange to the tool tip. The latter transform only consists of a translation along the z-axis. This is found empirically by bringing the pen tip to the origin of the whiteboard frame and solving for the error between the whiteboard frame origin and the flange position, both of which are known. This calibration procedure introduces a source of error in the resulting trajectory tracking accuracy.

Furthermore, the robot base frame is calibrated in the QTM software empirically. This means that there is an error between the true robot base frame and the robot base frame measured by the motion capture system. This is another possible source of error in the accuracy of the system. To get an idea of the magnitude of the resulting error, a calibration error of 1° around the z-axis will result in approximately 0.017 m translational error in the end effector given that the end effector is 1 m away from the robot base.

Finally, it should be noted that the coordinate frame for which the hexapod platform generates the desired wave motions around was moved from the centre of the platform to the origin of the robot base frame empirically. Since the robot base is tracked independently, it will not introduce errors in tracking performance. However, this means that there is a small difference between the simulated vessel motions and the actual motions experienced by the robot base.

4. Results

To investigate the feasibility of active motion compensation of robotic arms on vessels at exposed locations, the end effector path shown in Fig. 7 was followed with desired speed $v_d = 0.08$ m/s. Results from four experiments are presented, in which the hexapod platform was driven according to the simulated vessel motions with environmental conditions as summarised in Table 2 and motion characteristics as shown in Table 3. The desired pose of the robotic arm end effector was computed according to Eq. (5) and updated at a frequency of 62.5 Hz.

The corresponding drawn paths for the four tests are shown in Fig. 9. The desired path and the path measured by the motion capture system are shown, as well as contrast-adjusted photos of the whiteboard drawings. It is seen that for the leftmost test with $H_S = 0.5$ m (EXP1), the reference is followed accurately, and as the significant wave height increases, so does the tracking error. The largest error is seen for EXP4, with $H_S = 2.0$ m, for which still images from a video recording of

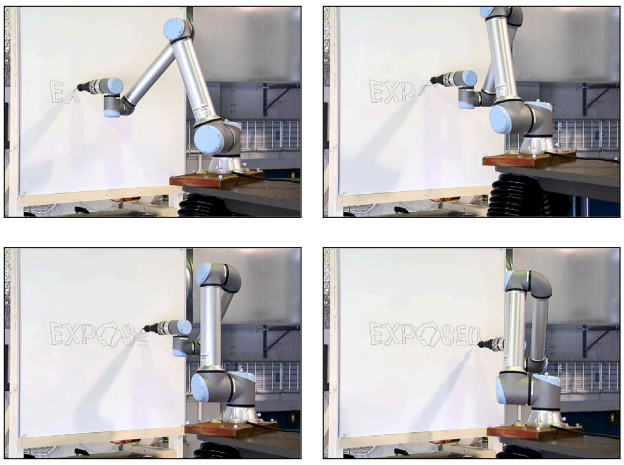

Fig. 8. Still images of EXP4 whiteboard writing test, showing the Sirocco motion hexapod, UR10e robot manipulator arm equipped with pen tool end effector and whiteboard.

the experiment are presented in Fig. 8. Supplementary video material showing the experimental results are made available.[8]

The remaining figures and quantitative results are presented in full scale. This entails that the raw experimental results have been scaled corresponding to how the hexapod data were initially scaled to fit the model scale, i.e., using a length factor of $\lambda = 4.84$ and a time factor of $\sqrt{\lambda} = 2.2$. For example, raw translation errors [m] have been scaled by a factor of λ, rotational errors [deg] have been left as is, and angular accelerations [deg/s^2] have been scaled by a factor of $1/\lambda$.

The translational and rotational tracking errors are shown over time for the four test cases in Fig. 10. The translational error is given by the Euclidean distance error

$$\Delta r = \left\| r^W_{WP} - r^W_{WP^\star} \right\|_2 , \tag{6}$$

with $\| \cdot \|_2$ denoting the 2-norm. The rotational error is given by the angular error

$$\Delta\theta = \arccos\left(\frac{\mathrm{tr}\left(R^W_P \, R^{W\,-1}_{P^\star} \right) - 1}{2} \right), \tag{7}$$

where $r^W_{WP^\star}$ and $R^W_{P^\star}$ define the desired position and rotation of the pen tool, respectively, r^W_{WP} and R^W_P define the actual position and rotation of the pen tool, respectively, and $\mathrm{tr}(\cdot)$ denotes the matrix trace. Average translational and rotational errors over the test durations are presented in Table 4, showing a clear increase in the tracking error for larger significant wave heights.

Finally, a relevant question is how large joint accelerations to expect and how this transfers to a full-scale maritime crane. Especially the first three joints of the robot manipulator, namely the base, shoulder and elbow joints, are of interest as they do most of the work in regards to tracking the position reference. As such they are quite analogous to a typical offshore knuckle-boom crane with 3 joints. In Fig. 11 a box-and-whisker plot of the first three joint accelerations is shown for the test cases in full scale.

5. Discussion

As expected, the robotic arm performs well as long as the vessel motions are slow. For all experiments EXP1–EXP4 we see that the average translational and rotational tracking errors are less or equal to 3 cm and 0.139° (see Table 4), respectively. We believe that this is within a sufficient accuracy range to perform, for example, a terminal connection operation, although specific requirements will need further investigations.

For sea states of increasing intensity, higher accelerations were imposed and a time delay and corresponding tracking error were observed. The tracking error and time delay are discussed further in the following, and a discussion of open problems relating to robotic arm design and sensors for full-scale tests is given.

Table 4
Average (± std) translational (Δr, scaled by λ) and rotational ($\Delta\theta$, not scaled) tracking errors for each experiment.

	Δr [m]	$\Delta\theta$ [deg]
EXP1	0.013 ± 0.005	0.060 ± 0.029
EXP2	0.018 ± 0.008	0.120 ± 0.055
EXP3	0.024 ± 0.012	0.120 ± 0.062
EXP4	0.030 ± 0.016	0.139 ± 0.075

Table 5
Empirical correlation coefficients between hexapod speeds and end effector tracking errors, for EXP1-EXP4.

		$\|v\|$ [m/s]	$\|\omega\|$ [deg/s]
EXP1	Δr	0.12	−0.02
	$\Delta\theta$	0.56	0.96
EXP2	Δr	0.53	0.17
	$\Delta\theta$	0.54	0.97
EXP3	Δr	0.71	0.18
	$\Delta\theta$	0.49	0.97
EXP4	Δr	0.84	0.24
	$\Delta\theta$	0.50	0.98

5.1. Error analysis

The error in the observed pose is dependent on the speed of the hexapod and the reference trajectory. To investigate this dependency, the end effector pose error is broken down into two components, the positional error (Euclidean distance of shortest correcting translation) and the rotational error (angle of shortest correcting rotation). Similarly, we distinguish between the linear and angular speed of the hexapod, both computed with finite differences over the hexapod input data.

Since the measurements of the end effector and the input data used by the hexapod come from two different systems, the two time series had to be synchronised before further analysis could be made. For each experiment, two parameters were estimated; the offset in start time and the difference in sample rate. Differences in start time varied between experiments because the hexapod and robotic arm were launched independently. The discrepancy in sample rate was also empirically estimated to account for delays in the manipulator's control loop. Both parameters were estimated for each experiment using a fine-grained grid search around initial guesses inferred from visual inspection. Afterwards, the hexapod speed values were resampled with linear interpolation to produce one value for each end effector error measurement.

Fig. 12 shows the translational and rotational errors plotted against the linear and angular hexapod speeds for the EXP4 experiment. Corresponding results for all experiments are summarised with their empirical correlation coefficients in Table 5. It is seen that there is a correlation between higher velocities and larger tracking errors, especially between angular velocity and error. It was theorised that these errors are primarily caused by time delays, which is further detailed in the following.

[8] https://youtu.be/rDLI80Z2BnM
https://youtu.be/WjfGDu3APtI.

Fig. 9. Comparison between reference and measured trajectories. The top row shows the reference trajectory (orange) along with the trajectory measured by the motion capture system (blue). The bottom row displays contrast adjusted photographs of the resulting drawings.

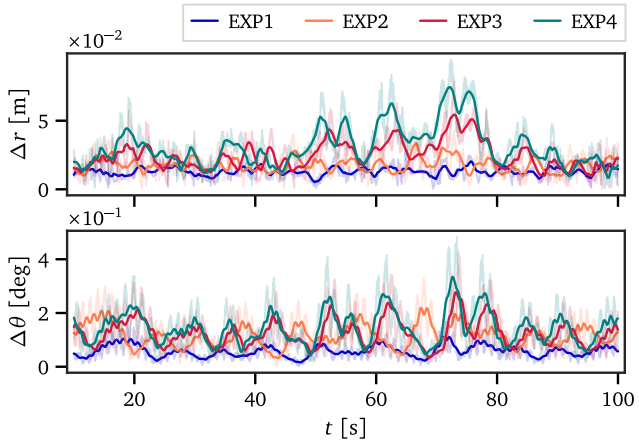

Fig. 10. Translational (Δr, scaled by λ) and rotational ($\Delta\theta$, scaled $\times 1$) tracking error between desired and measured end effector pose. Solid lines represent a 100-sample (1.6 s) moving average, the raw data can be seen in the background.

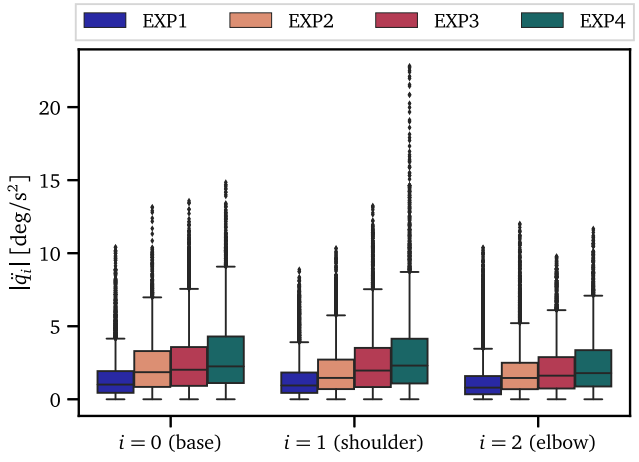

Fig. 11. Absolute joint acceleration ($|\ddot{q}_i|$, scaled by $1/\lambda$) in full-scale for the first three joints of the UR10e robot manipulator arm between $t = 10$ s and $t = 100$ s.

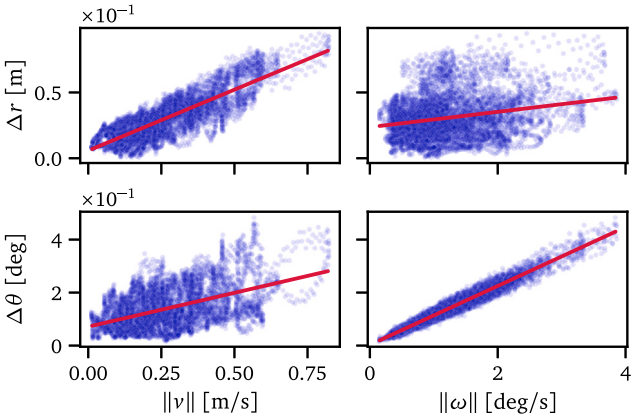

Fig. 12. Translational (Δr, scaled by λ) and rotational ($\Delta\theta$, not scaled) tracking error versus hexapod linear ($\|v\|$, scaled by $\sqrt{\lambda}$) and angular ($\|\omega\|$, scaled by $1/\sqrt{\lambda}$) speed for the EXP4 experiment. Red lines indicate the linear regression fit for the data.

5.2. Time delay

A significant source of error for motion compensation of autonomous cranes is time delay. This had a large impact on the presented results, as apparent by the preceding error analysis (see Fig. 12), indicating large tracking errors being observed for large velocities. This is explained by the fact that a higher velocity results in larger spatial lag for a given time delay, and thus larger tracking error. The time scaling as discussed in Section 2.5 amplified the needed velocities in order to ensure realistic accelerations, and thus also amplifies the errors caused by time delay.

There is a small latency in the motion capture system and a computation delay in the software developed to generate the desired pose references. However, the dominating factor for the present tests was found to be the actuation delay in the UR10e robotic arm. The internal controller of the UR10e smooths the trajectory with a minimum time window of 30 ms, which limits the achievable accuracy for real-time critical applications such as the present problem.

Testing alternative hardware is a possible way around this. However, smoothing is beneficial for safety reasons and to limit wear and tear on the actuators. Another possibility may be to use an alternative scaling method, possibly by scaling space but not time. This would lead to slower translational and rotational motions in the model scale test setup, but will not satisfy the requirements of achieving comparable translational accelerations. However, the fact of not being able to similarly scale the delay will lead to the requirement of minimising the scale factor by designing a model test setup as close as possible to full scale size.

Predicting the 6 DOF motion of the robot base is a more realistic option for counteracting the system's time delay. The duration of the time delay can be estimated by cross-correlating the reference and measured signals. The motion prediction could, e.g., be done with an extended Kalman filter or an unscented Kalman filter, or more simply by propagating the current state with a constant velocity or constant acceleration model. As discussed in From et al. (2011), the system could even use this prediction to its advantage when motion planning to reduce the total torque needed. It is believed that lower tracking errors than what was shown in Table 4 can be achieved if prediction methods are used to mitigate the impact of the actuation delay, which will be investigated in future work.

5.3. Open problems and next steps

In order to automate aquaculture operations as listed in the Appendix, a number of open problems, not being investigated in this paper, remain. First of all, we have not investigated the design of a robotic arm, for instance, the optimal length of the arm to carry out the operation. This will depend on the operation, the vessel design, placement of the robotic arm, and the desired proximity of the vessel to the cage. For the latter, important aspects are the effect of the propulsion system on fish welfare and the integrity of the net structure.

Due to safety reasons, to drift away in case of a blackout, a vessel should always operate on the lee side of the cage. The effect of the propeller slip stream blowing into the cage might therefore be negligible. However, how to detect the distance to the net below the water surface must be investigated.

Secondly, the UR10e robotic arm used in the experiments will have several design-related differences from a robotic arm used in real aquaculture operations, as visualised in Fig. 4. Besides proportional differences, the robotic arm configuration, weight, flexibility, speed, etc. will differ. As can be seen from Fig. 11, the robotic arm did not require too large joint accelerations. For a possibly heavier arm, larger accelerations will require a higher degree of structural integrity of the arm. Whether these results are within the design limitations of such an arm is outside the scope of this work, and will need further investigation. Furthermore, longer links will lead to higher structural elasticity of lower eigenfrequencies. In this context, vibration will be of interest, also related to its impact on the control system and its accuracy level, regarding the feasibility of obtaining a level of accuracy comparable to that reported in Table 4. To investigate the magnitude and effect of elasticity and ensure that possible deviations from the assumption of rigid links, e.g., when calculating the inverse kinematics, will not result in increased errors, further full-scale modelling and tests are needed.

Performing defined work tasks and manipulating objects in or on the cage structure will require the ability to detect and track defined objects. The choice and use of sensors, such as inertial measurements (IMUs), global navigation satellite systems (GNSSs), cameras, lasers, and lidars must be investigated. The selected sensor suite needs to account for varying lighting conditions, fast motion and rough environmental conditions. Time delay and synchronisation errors will lead to degraded trajectory tracking performance and should therefore be limited as much as possible. The needed redundancy will require additional sensor systems, also needed to realise collision avoidance.

The placement of expensive sensor equipment in or on the cage structure should be avoided, as these typically will need to be removed after the operation is finished. To be able to permanently install the marker or sensor on the facility, the equipment should be simple and affordable. In this work, sensor related challenges and solutions were not specifically investigated.

Since both the vessel and fish cage are in motion, it might be necessary to predict the motion (maybe the next 100 ms) using a Kalman filter or similar (as discussed in Section 5.2). Similarly, motion of objects to be grasped and manipulated could be predicted with a combination of measurements and models. Accurate predictions could, to some extent, compensate for sensor delay.

Another challenge is that most of the operations in Appendix are manual, and were not designed with automation in mind. Hence, a particular challenge will be to design the mechanical interface between the robotic arm and the objects to be grasped or manipulated. Also, as mentioned in the beginning of this section, the position, orientation, and error requirements for terminal connection operations must be specified. Although the trajectory tracking error results presented in this work seem promising, no specifications on how to evaluate the results are published.

As discussed in Section 5.2, time delays can have a large impact on the results and will contribute to the definition of the operational limitation criterion with regards to maximum allowed relative motions. The use of different types of sensors will make handling of time delays and time synchronisation even more important. Therefore, a key aspect of further development will be the achievement of general robustness by the integration of various sensor data, improving redundancy to sensor failures, while ensuring fast response times and short delays in the system.

6. Conclusion

The feasibility of performing contact-free aquaculture operations using a robotic arm mounted on the deck of a service vessel was investigated. The motion behaviour of a modern aquaculture service vessel under DP for four different sea states was simulated and used as input for the evaluation of the feasibility of using a robotic arm for regular work tasks at a conventional aquaculture facility. An experimental setup with a robotic arm placed on a hexapod platform, simulating vessel motions, was used to evaluate to what degree the robotic arm was able to follow a reference trajectory. Results of the performance analysis were illustrated by figures of the translational and rotational errors of the end effector, as well as absolute accelerations for base, shoulder, and elbow joints. The robotic arm performed well as long as vessel motions were slow. With increasing sea state, tracking errors caused by time delay were observed. Due to the selected scaling method (Froude scaling), giving similar mass forces as in full scale, translational speed, as well as rotational angular rate and acceleration, were increased. This caused larger trajectory tracking errors of the end effector in model scale than what would be expected in a full-scale setup.

Although the results, in general, are promising, further questions, as summarised in this work, are needed to be assessed before contact-free aquaculture operation becomes a feasible alternative to the hazardous manual work on the collar of the facility. A weatherproof, robust and redundant sensor setup must be developed. Similarly, full-scale tests with a prototype of a robotic arm are needed to evaluate structural stiffness and the structural behaviour of the joints when operating under load. Finally, tools must be designed to be used as end effectors, enabling the robotic arm to perform the intended work tasks.

CRediT authorship contribution statement

Martin Albertsen Brandt: Methodology, Software, Investigation, Writing, Visualization. **Sverre Herland:** Methodology, Software, Investigation, Writing, Visualization. **Martin Gutsch:** Conceptualization, Methodology, Formal analysis, Investigation, Writing. **Halgeir Ludvigsen:** Methodology, Formal analysis, Investigation, Writing. **Esten Ingar Grøtli:** Conceptualization, Writing, Supervision, Project administration.

Declaration of competing interest

The authors declare that they have no known competing financial interests or personal relationships that could have appeared to influence the work reported in this paper.

Data availability

Data will be made available on request.

Acknowledgements

We thank the mechanical workshop at SINTEF Ocean for assistance in the assembly of the experimental setup. This work was funded by The Research Council of Norway (RCN) through the Center for Research-based Innovation Exposed Aquaculture Operations (RCN project number 237790).

Appendix. Overview of a selection of work operations

A selection of work operations on offshore fish cage sites is presented in Table 6.

Table 6
Selection of work operations on offshore fish cage sites (Misund and Gutsch, 2020).

Regularity	Operation	Equipment	Location	Personnel required
Daily	Dead fish collection/removal	Pump, dewatering container, crane. Basket, hand net, capstan, crane.	Net pens	2
	Net cage maintenance	Knife, rope, (in some cases capstans and cranes)	Net pens, floating collar, walkway, railings	1–2
Weekly	Counting salmon lice	Seine, crane, capstan, sedatives, seawater container, hand net	Net pens	2–4
Monthly (season based)	Placing and maintenance of wrasse shelter	Crane, high pressure washer	Net pens	2
Quarterly	Feeding tube handling/maintenance	Saw, ropes, straps, coupling, knife, gaskets	Net pens, barges, between the pens and barge	> 2
Yearly or rarer	Net installation	Crane, winch	Net pens, railing, collar	3–4
	Inspection of moorings	ROV, crane	Mooring grid system	> 2
Operation dependent	Handling of sinker tube	Crane, straps	Net pens	> 2
	Installation of bottom net weight	Crane, capstan, ropes	Net pens, collar	> 2
	Receiving wrasse	Container (maybe crane)	Net pens	2
	Inspection of the cage net	ROV, needle, thread	Net pens	> 2
	Transportation of equipment	Crane	Barge, Net pens	> 2
	Delousing operations	Mechanical, thermal, tarpaulin, triplex, oxygen equipment, seines, ball line, crane, capstan	Net pens, well boats	> 5
	Deliveries/sorting/splitting	Seines, ball line, crane, capstan	Well boat, net pens	> 5
	Feeding pipes to feeding selector valve	Straps, rope, knife, various hand tools	Barge	1–2
Seasonal dependent	Installing of lights	Knife, rope	Net pens	> 2
	Cleaning of net	ROV	Net pens	2–4
	Cleaning and disinfecting equipment	ROV	Net pens	2–4

References

Bjelland, H.V., Føre, M., Lader, P., Kristiansen, D., Holmen, I.M., Fredheim, A., Grøtli, E.I., Fathi, D.E., Oppedal, F., Utne, I.B., Schjølberg, I., 2015. Exposed aquaculture in Norway. In: OCEANS 2015 - MTS/IEEE Washington.

Cao, Y., Li, T., 2020. Review of antiswing control of shipboard cranes. IEEE/CAA J. Autom. Sin. 7, 346–354.

Fathi, D., 2012. SHIPX Vessel Responses (VERES) - Ship Motions and Global Loads, User Manual. MARINTEK Report.

Faulwasser, T., Weber, T., Zometa, P., Findeisen, R., 2017. Implementation of nonlinear model predictive path-following control for an industrial robot. IEEE Trans. Control Syst. Technol. 25 (4), 1505–1511.

From, P.J., Gravdahl, J.T., Lillehagen, T., Abbeel, P., 2011. Motion planning and control of robotic manipulators on seaborne platforms. Control Eng. Pract. 19 (8), 809–819.

Himeno, Y., 1981. Prediction of Ship Roll Damping-State of the Art. Technical Report, University of Michigan.

Holmen, I., Utne, I., Haugen, S., 2017. Organisational safety indicators in aquaculture—A preliminary study. In: Risk, Reliability and Safety: Innovating Theory and Practice - Proceedings of the 26th European Safety and Reliability Conference, ESREL 2016. p. 295.

Ikeda, Y., Himeno, Y., Tanaka, N., 1977. On eddy making component of roll damping force on naked hull. J. Soc. Nav. Archit. Japan 1977 (142), 54–64.

Kato, H., 1957. On the frictional resistance to the rolling of ships. J. Zosen Kiokai 1957 (102), 115–122.

Misund, A.U., Gutsch, M., 2020. Contact Free Operations: Description of Work Operation in Aquaculture. Technical report. SINTEF Ocean - SFI Exposed, SINTEF Ocean - SFI Exposed.

Norwegian Ministry of Trade, Industry and Fisheries, 2015. Forskrift om bygging OG tilsyn AV mindre lasteskip. Lovdata, URL: https://lovdata.no/dokument/SF/forskrift/2014-12-19-1853.

Ramm, H.T., Berge, A.W., 2017. Fleet Scheduling of Service Vessels Used in a More Exposed Norwegian Aquaculture Industry (Master's thesis). Norwegian University of Science and Technology.

Reite, K.-J., Føre, M., Aarsæther, K.G., Jensen, J., Rundtop, P., Kyllingstad, L.T., Endresen, P.C., Kristiansen, D., Johansen, V., Fredheim, A., 2014. Fhsim—time domain simulation of marine systems. In: International Conference on Offshore Mechanics and Arctic Engineering, Vol. 45509. American Society of Mechanical Engineers.

Salvesen, N., Tuck, E., Faltinsen, O., 1970. Ship motions and sea loads. Trans. SNAME 78, 250–287.

Shoemake, K., 1985. Animating rotation with quaternion curves. In: Proceedings of the 12th Annual Conference on Computer Graphics and Interactive Techniques. pp. 245–254.

Sun, N., Fang, Y., Chen, H., Fu, Y., Lu, B., 2018. Nonlinear stabilizing control for ship-mounted cranes with ship roll and heave movements: Design, analysis, and experiments. IEEE Trans. Syst. Man Cybern.: Systems 48 (10), 1781–1793.

Tørdal, S.S., Hovland, G., 2017. Inverse kinematic control of an industrial robot used in vessel-to-vessel motion compensation. In: 2017 25th Mediterranean Conference on Control and Automation. MED, pp. 1392–1397.

Tysse, G.O., Cibicik, A., Tingelstad, L., Egeland, O., 2022. Lyapunov-based damping controller with nonlinear MPC control of payload position for a knuckle boom crane. Automatica 140, 110219.

Utne, I.B., Sørensen, A.J., Schjølberg, I., 2017. Risk Management of Autonomous Marine Systems and Operations. In: ASME 2017 36th International Conference on Ocean, Offshore and Arctic Engineering, Vol. 3B: Structures, Safety and Reliability.